PKS0407-65: Field structure and polarization properties

Benjamin Hugo, Griffin Foster, Marisa Geyer, Oleg Smirnov,
Thomas Abbott and Ksjitij Thorat

April 2018

Abstract

PKS0407-65, along with PKS1934-638, is one of two primary calibrators used for calibrating MeerKAT's direction-independent, frequency-dependent instrumental response. Traditional calibration makes the simplifying assumption that such fields can be well-approximated by a single delta-function source. In this memo, we show that the presence of faint secondary sources dominates instrumental calibration error. We also investigate the polarization properties of PKS0407-65 and show that this compact source is polarized at the 0.5% level. Both the surrounding field, as well as the polarization properties of the primary calibrators have to be taken into account during direction-independent calibration of the tied-array beamformer.

1 Revision List

- Version 1: April 2018, initial version with substructure model and polarization characteristics of 0407-65.
- Version 1.1: July 2018, typo fixes

2 Introduction

MeerKAT beamformer calibration is done prior to observation, using the planned MeerKAT signal processing chain depicted in Figure 2. In this chain the beamformer data are corrected for time and frequency-variable effects, using interferometric (per antenna) gains, some of which are derived immediately prior to observation. The time-dependent phase variations and signal chain delays on X and Y are two prime examples. It is critically assumed that these time-dependent gains are stable over the course of a beamformer observation and that the calibration is correct: unlike in imaging observations there is no possibility for self-calibrating data after capture.

Beamformer gain and polarization calibration is essential to maximize the efficiency of the tied-array beams, thus improving the sensitivity of pulsar search and timing surveys. Intrinsic polarization leakage of the receiver feeds affects our ability to do pulsar timing. Calibration errors of a few percent can result in microsecond-level errors at leakages above -15dB [Foster et al., 2015]. Using full Stokes data for timing allows for an improvement in Time-of-Arrival (ToA) estimation over total intensity-only timing. This can best be done with a well-calibrated system. The polarization leakage can be partially corrected for by deriving a polarization leakage term from interferometric observations and applying this term to timing observations. This is a significant advantage of arrays over single dish telescopes. This leakage is expected to be stable on week-month time scales and it is planned to derive solutions with our FleetingPol pipeline depicted in Figure 1. Gain calibration, on a coherent phase time-scale (this time scale is still to be determined), allows for the formation of coherent beams, maximizing the beam sensitivity. This calibration time scale is not covered in this report.

Currently the X and Y amplitude responses (per frequency) are corrected for using either PKS 1934-638 or PKS 0407-65. These sources sets the flux scale of both the X and B-engine data. The calibration has to be done just prior to beamformer observation due to current limitations in the SDP calibration pipeline: currently calibrating for electronic differential gains and the per channel bandpass response are tied. The derived per frequency instrumental gains have been shown to be stable on the -25 to -26dB level over the span of several hours in 208kHz channelization mode and need not be re-calibrated for on such regular intervals: a significant portion of telescope time (a

minimum of 15 to 20min) is typically needed to reach the necessary SNR for these fine-grained solutions and wash out RFI.

This report deals with sources of calibration error stemming from improper modeling of the primary flux calibrators. We will show that if the polarization of the primary source and the flux contributions of secondary sources in such a field are neglected, the calibration solutions for X and Y are biased. As these solutions are ultimately transferred to timing observations, they introduce biases between XX and YY which are dependent on the epoch at which the primary calibrator was observed. We will specifically look at modeling the polarization, as well as the secondary sources around PKS 0407-65 to avoid such errors.

3 Main sources of calibration error

Interferometric arrays, whether product ("correlation") interferometers or addition ("beamforming") interferometers, measure the spatial frequency domain in short-time averages. The two styles of interferometers are equivalent provided the input signal can be coherently measured between antenna pairs p and q (GSF: they aren't equivalent, beamforming is equivalent to summing all the correlation products). This is true if the source is at the tracking centre of the telescope, in the absence of instrumental and environmental effects. Arguably the only, slight, difference in our case is that our beamformer produces an average power from N_{ant} measurements, whereas the correlator produces $\frac{N_{\text{ant}}(N_{\text{ant}}-1)}{2}$ individual averages, which could be stacked to a single average power, as in the case of the former. The calibration errors we discuss here are not random and have to be eliminated; they will not necessarily diminish through averaging.

The Cittert-Van Zernike relation establishes the relation between the sky brightness distribution ($I_{\text{true}}(l,m)$) and the spatial frequency domain ($V_{\text{true}}(u,v,w)$) measured by a two-element interferometer, in the absence of any instrumental or environmental effects:

$$V_{\text{true}}(u(H,\delta),v(H,\delta),\nu) = \int\int I_{\text{true}} e^{-2i\frac{\nu}{c}\pi(ul+vm+w(\sqrt{1-l^2-m^2}-1))} \frac{dldm}{\sqrt{1-l^2-m^2}}$$

Here l and m are direction cosines off a coordinate frame where w points towards the phase tracking centre (normally the pointing centre) of the telescope. Under the simplifying assumption that the measurements are all coplanar the relationship can be expressed as a classical two-dimensional Fourier transform. Such a two-dimensional description holds for all east-west interferometers, such as the Westerbork Synthesis Radio Telescope. Interferometers with non-east-west components such as the VLA and MeerKAT can be modeled with the full two-to-three dimensional relationship detailed above.

Traditional direction independent interferometric calibration attempts to solve for, respectively, time- and frequency-variable instrumental and environmental gains (assuming an additive zero-mean Gaussian noise, ϵ). For the moment assume that such gains are expressed as g_p, g_q (complex) per-antenna terms for a single feed system to simplify the expression. The visibility observed by antennas p and q is then:

$$V_{\text{obs}}(u(H,\delta),v(H,\delta)) \approx g_p(H,\nu)g_q^*(H,\nu)V_{\text{true}}(u(H,\delta),v(H,\delta),\nu) + \epsilon$$

Under the assumption that the system frequency response is stable over extended periods of time, these gains can be separated into time- and frequency-variable functions and solved for in a classical least squares fashion at regular time- and frequency-intervals by combining all baselines observed within these intervals, minimizing χ^2. The real and imaginary components can be treated separately to keep things simple. Here $([i,j],[k,l])$ are arbitrary time- and frequency intervals respectively:

$$\chi^2(i \le H \le j, k \le \nu \le l) = \sum_{u,v=\text{bl}(H,\delta,\nu)} \left| V_{\text{obs}}(u,v) - g_p(\nu)g_q^*(\nu)g_p(H)g_q^*(H)V_{\text{model}}(u,v) \right|^2$$

V_{model} is the two-to-three-dimensional transform of a sky model, I_{model}. This process assumes that the input sky model is a good approximation of the true sky, I_{true}. Any real emission that is not included in the model will, to some extent, be absorbed into these time and frequency gains. The exact extent to which they are absorbed depends on how frequently solutions are computed: time and frequency variations are washed out by time and bandwidth smearing. These variations in gains is a source of calibration error if the gains are transferred to a target field.

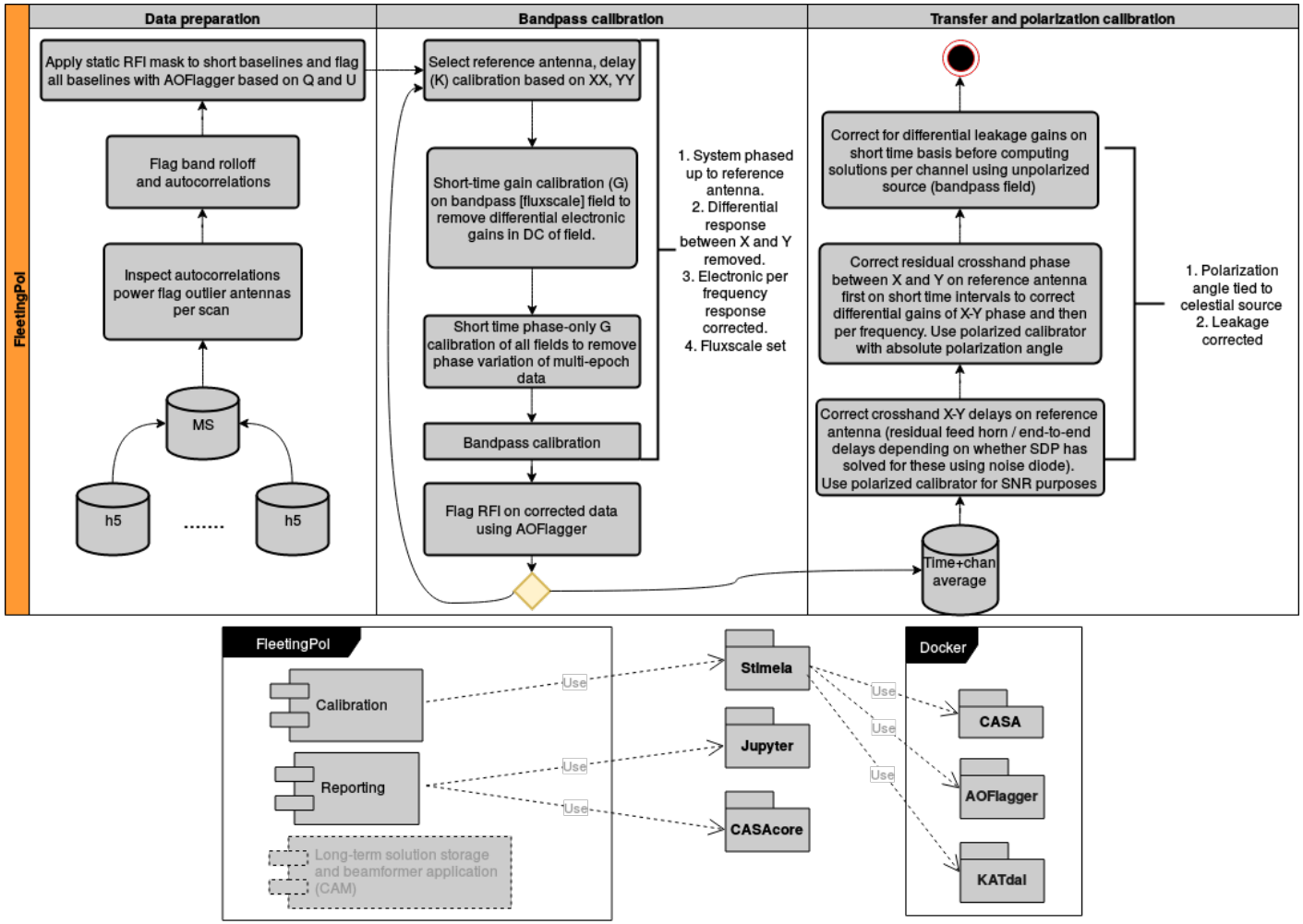

Figure 1: RARG FleetingPol pipeline used for deriving polarization solutions and quality assurance reporting. The pipeline is built using the Stimela scripting framework, which containerizes pipeline steps using Docker™. Package is available from https://github.com/ska-sa/fleeting-pol, email to request access.

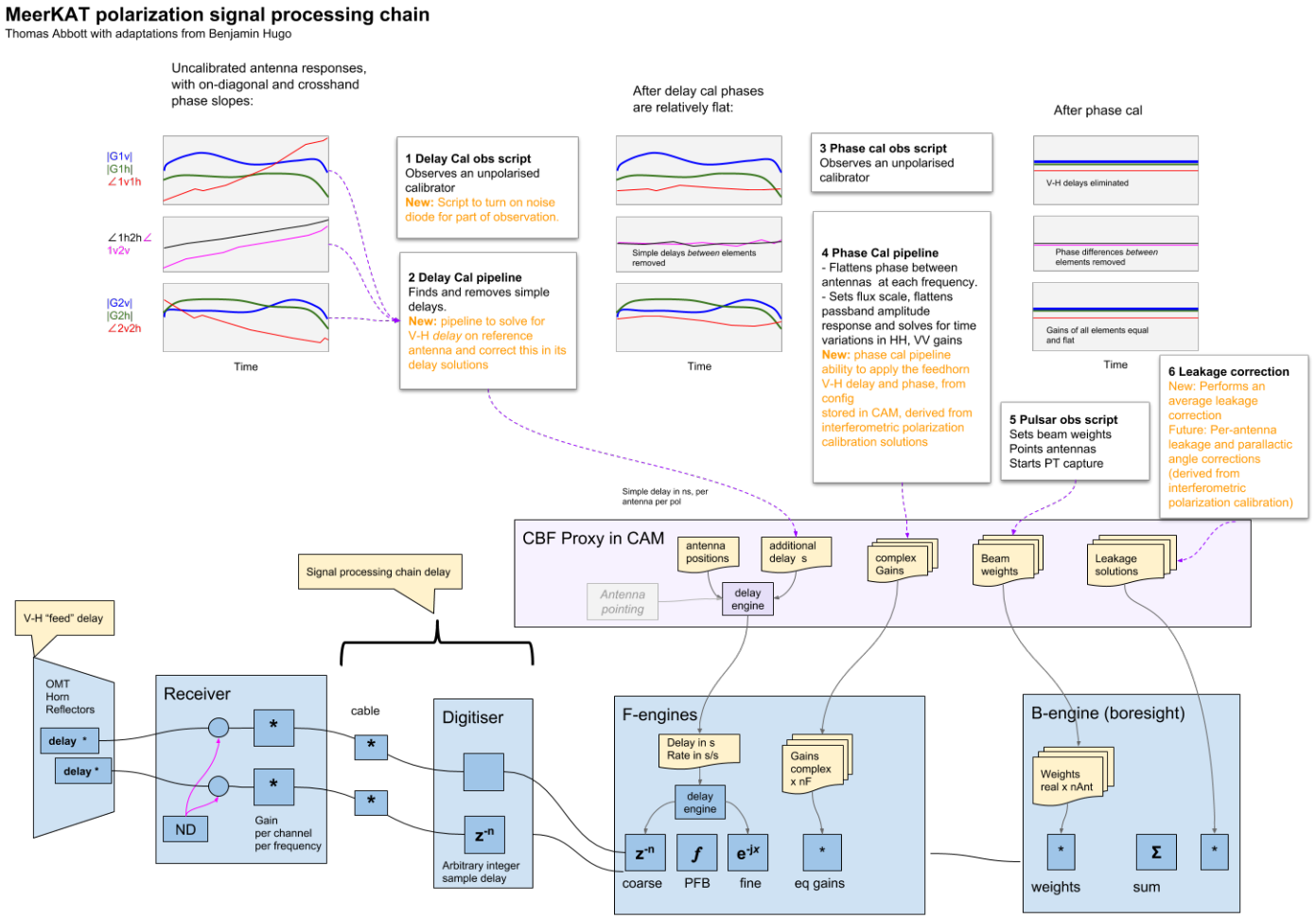

Figure 2: Planned MeerKAT beamformer signal processing chain. This figure depicts the calibration challenges faced with beamformed data. There are two primary sources of delay, which we will refer to as "feed horn delays", actual delays induced by the distance between dipoles, for instance, and "signal chain delays". The signal chain delays are solved for first using a stabilized noise diode behind the horn, where after the feed horn delays are solved for using a celestial polarized calibrator with known polarization angle. The signal chain delays are not stable and can vary between subarray builds if the reference antenna is changed or the digitizers are re-synced, while the feed horn delays should remain stable. Currently only average corrections for leakages can be applied.

Traditionally, secondary sources in the calibrator fields that are at the $\leq\approx 5\%$ level of the calibrator, are ignored. As typical bandpass calibrators have L-band flux densities of some 10s Jy, the flux density of the secondary sources are likely to be in the 10s-of-mJy range. The only requirement that is imposed in such simple approach is that the calibrator has to be unresolved. Ignoring substructure at these levels can ultimately prove to be a limiting factor to the dynamic range achievable in deep spectral imaging mode observations and pulsar timing experiments, where stability and minimal leakages are key considerations.

The error can be described at the hand of a simple example. If some fictitious calibrator field consists of only a point-source and a second fainter source in close proximity, the visibilities will contain ripples instead of a smooth curve over the passband. To see why we simply consider the analytical expression of the Fourier transform of two unresolved point sources. The primary source is at phase centre, the other is at some coordinate $(x_i, 0)$ on the celestial sphere, but well-within the primary beams of the antennae. The two sources have apparent flux densities S_0 and S_1 respectively:

$$
\begin{aligned}
V(u(H,\nu), v(H,\nu)) &= S_0 + S_1 e^{-2\pi i (u(H,\nu) x_1)} \\
\implies ||V(u(H,\nu), v(H,\nu))||^2 &= S_0^2 + S_1^2 + 2 S_0^2 S_1^2 \cos(2\pi x_1 u(H,\nu) \\
\implies \arg(V(u(H,\nu), v(H,\nu))) &\approx \tan^{-1}\left(\frac{S_1 \sin\left(-2\pi x_1 u(H,\nu)\right)}{S_0}\right) (S_0 \gg S_1)
\end{aligned}
$$

This periodic variation in the visibility amplitude and phase, the "ripple", is time- and frequency dependent. It has a period that increases with decreasing baseline length and the source distance from phase centre. This ripple is real emission. If the calibration model fails to include the second source the model error propagates as time, frequency-dependent calibration errors into the gains. Furthermore they will serve to worsen the apparent system leakage. This variation is undesirable, but will go away if the calibration is based on a more complete local sky model.

In reality the interferometric array records all combinations of X and Y feeds. Each type of direction independent calibration error (aside from closure errors) can be expressed as a chain of Mueller screens (GSF: Mueller screens? I don't know what these are) $J_{pq} = J_p \bigotimes J_q^*$, where J_p and J_q are per antenna Jones matricies: $V_{\text{obs}} = J_{pq,1} J_{pq,2} \ldots J_{pq,N} V_{\text{true}}$. $J_{pq,1}$ is the systematic or environmental effect closest to the correlator, for example the electronic bandpass response, and $J_{pq,N}$ is the effect furthest from the correlator, say parallactic rotation. See[Smirnov, 2011] and the references therein for details. The most prominent ones we will consider for discussion are:

- **B** frequency-dependent, time-independent instrumental "bandpass" response.
- **G** frequency-independent, time-dependent instrumental differential "gain".
- **X** crosshand delay, which can be separated further into a phase and delay term
- **D** instrumental leakage due to the physical nature of the feed, e.g, feed-misalignment, projection, and response.
- **P** sky rotation around the pointing direction resulting from alt-az mounts (parallactic angle).

If ψ represents parallactic angle, assuming an alt-az mount, ρ crosshand phase and I, Q, U, V are time, declination and frequency-dependent visibility Stokes components. Following [Hales, 2017] first order terms of the system response in the presence of leakage ($\mathbf{GBXDP}V_{\text{true}}$) can be described by the following set of equations:

$$
\begin{aligned}
V_{\text{XX}}^{\text{obs}} &= g_{X_p}(H,\nu) g_{X_q}^*(H,\nu)((I + Q_\psi) + U_\psi(d_{X_p} + d_{X_q}^*)) \\
V_{\text{XY}}^{\text{obs}} &= g_{X_p}(H,\nu) g_{Y_q}^*(H,\nu) \left[(U_\psi + iV) + I(d_{X_p} + d_{Y_q}^*) - Q_\psi(d_{X_p} - d_{Y_q}^*)\right] e^{i\rho} \\
V_{\text{YX}}^{\text{obs}} &= g_{Y_p}(H,\nu) g_{X_q}^*(H,\nu) \left[(U_\psi - iV) + I(d_{Y_p} + d_{X_q}^*) + Q_\psi(d_{Y_p} - d_{X_q}^*)\right] e^{-i\rho} \\
V_{\text{YY}}^{\text{obs}} &= g_{Y_p}(H,\nu) g_{Y_q}^*(H,\nu)((I - Q_\psi) + U_\psi(d_{Y_p} + d_{Y_q}^*)) \\
U_\psi &:= U\cos(2\psi) - Q\sin(2\psi) \\
Q_\psi &:= Q\cos(2\psi) + U\sin(2\psi)
\end{aligned}
$$

If there is a time and frequency residual error $(1+\xi_{X_{pq}}(H(\text{epoch}),\nu))$, $(1+\xi_{Y_{pq}}(H(\text{epoch}),\nu))$,$(1+\xi_{XY_{pq}}(H(\text{epoch}),\nu))$ and $(1+\xi_{YX_{pq}}(H(\text{epoch}),\nu))$ resulting from applying erroneous calibration $\mathbf{B}_\xi^{-1}\mathbf{G}_\xi^{-1}\mathbf{GB}$ then the apparent leakages, as well as the true contribution from Q_ψ are increased:

$$
\begin{aligned}
V_{\mathrm{XX}}^{\mathbf{BG}} &= (1+\xi_{X_{pq}}(H(\text{epoch}),\nu))((I+Q_\psi)+U_\psi(d_{X_p}+d^*_{X_q})) \\
V_{\mathrm{XY}}^{\mathbf{BG}} &= (1+\xi_{XY_{pq}}(H(\text{epoch}),\nu))\left[(U_\psi+iV)+I(d_{X_p}+d^*_{Y_q})-Q_\psi(d_{X_p}-d^*_{Y_q}))\right]e^{i\rho} \\
V_{\mathrm{YX}}^{\mathbf{BG}} &= (1+\xi_{YX_{pq}}(H(\text{epoch}),\nu))\left[(U_\psi-iV)+I(d_{Y_p}+d^*_{X_q})+Q_\psi(d_{Y_p}-d^*_{X_q}))\right]e^{-i\rho} \\
V_{\mathrm{YY}}^{\mathbf{BG}} &= (1+\xi_{Y_{pq}}(H(\text{epoch}),\nu))((I-Q_\psi)+U_\psi(d_{Y_p}+d^*_{Y_q}))
\end{aligned}
$$

We see the following potential first order calibration error risks, in rank of severity, depending on the properties of the primary calibrator:

1. A difference in amplitude between X and Y feed gains if the bandpass and time-variable gains are not corrected for. This problem has been recently been solved and is part of the main SDP calibration pipeline.

2. Field substructure only partially modeled with a sky model will introduce variations on the bandpass solutions.

3. Failure to take the polarization of the primary calibrator into account. This introduces a epoch-dependent error in the X and Y bandpass gains on the order of $\pm Q^{\text{primary}}_{\psi(\text{epoch})}$.

4. Failure to take parallactic angle rotation of the target or calibrators into account. If Q_ψ and U_ψ are not corrected for parallactic angle then the XX and YY correlations will depend on hour angle. Unless timing polarized pulsars in Stokes I (XX - YY) this will result in biases. Importantly this holds true when only using single correlation data for timing experiments as well. Currently the MeerKAT correlator cannot correct for parallactic angle. This is a known limitation and will be addressed in future releases of the correlator software.

5. Failure to correct for leakage terms. Currently only an "average" array-wide leakage term can be corrected for at the start of beamforming observations due to a deficiency in the correlator software. This is known and will be addressed in subsequent improvements to the correlator software. The only foreseeable intermediate risks here are:

   - that leakage vary between different antennae which could be the result of improperly mounted feeds or distortions in the either of the reflectors, and/or
   - that the leakage is time or elevation dependent. We have shown that there is little dependence on elevation above 30 degrees. We note, however, that structure can clearly be seen on leakage solutions at lower elevations.

4 RM synthesis overview

Another topic that is relevant to modeling polarization of calibrators is RM synthesis. The observed polarization angle of a source may have been subject to Faraday rotation as it propagates along the line of sight of the observer. Here we assume the intrinsic polarization angle is subject to classical $\phi\lambda^2$ rotation model, where ϕ is measured in rad m^{-2}. Let $P(\lambda^2) = I(\lambda^2)\rho(\lambda^2)e^{2i\alpha}$ be the total linearly polarized flux density stemming from a source, where $\alpha = \frac{1}{2}\tan^{-1}\left(\frac{U}{Q}\right)$ is the source polarization angle and $\rho(\lambda^2) = \frac{U^2+Q^2}{I^2}$, the fraction of polarized emission. Much of the discussion here is drawn from [Burn, 1966] and [Brentjens and De Bruyn, 2005].

If the polarization angle is calculated by simply averaging the available bandwidth, the fraction of polarization is washed out, this is known as depolarization: the average of two complex numbers with different arguments, but the same magnitude, results in a number with smaller magnitude. However, provided the basic propagation model holds and the frequency resolution of the instrument is fine enough, the intrinsic polarization magnitude and angle can be recovered.

If the intervening medium between the observer and the source does not contribute to the overall flux density, but merely serve to rotate it and if α is independent of Faraday depth, we can

define the Faraday Dispersion Function as:

$$P_{\text{measured}}(\lambda^2) := \frac{\int_{-\infty,\infty} F(\phi) e^{2i\lambda^2\phi} d\phi \cdot w(\lambda^2)}{\int_{-\infty,\infty} F(\phi) d\phi}$$

with $w(\lambda^2) \in \mathbb{R} \mapsto \mathbb{R}$, the weighted sampling function in λ^2 space

and $R(\phi) := \frac{\int_{-\infty,\infty} w(\lambda^2) e^{-2i\phi\lambda^2} d\lambda^2}{\int_{-\infty,\infty} w(\lambda^2) d\lambda^2}$, the weighted response function in ϕ space

where $\phi = 0.81 \int_{0,\text{there}} n_e(\vec{r}) H_{||}(\vec{r}) d\vec{r}$, the Faraday depth with

$H_{||} \in \mathbb{R} \mapsto \mathbb{R}$, the projected induction

$$\text{let } K^{-1} = \int_{-\infty,\infty} w(\lambda^2) d\lambda^2 \int_{-\infty,\infty} F(\phi) d\phi$$

and substituting $(\exists u \in \mathbb{R})\lambda^2 = u\pi$

$$\begin{aligned}\text{then } F(\phi) * R(\phi) &= K^{-1} \int_{-\infty,\infty} P_{\text{measured}}(u\pi) w(u\pi) e^{-2\pi i u\phi} du \\ &= 2K^{-1} \int_{0,\infty} P_{\text{measured}}(u\pi) w(u\pi) e^{-2\pi i u\phi} du, \text{ assuming } F(\phi) * R(\phi) \text{ hermitian}\end{aligned}$$

$||F(\phi) * R(\phi)||$ yields the true polarization fraction after derotatation of the polarization angle (where ϕ is measured in m rad^{-2} along the line of sight). The normalization can be done assuming nothing in the medium between the observer and the source adds to the total flux of the source($\int I(u\pi) \approx \int F(\phi)$). This further implies that the fraction of intrinsic total linear polarization is preserved; the propagation medium simply induces rotation of the polarized electric field.

To compute $F(\phi) * R(\phi)$ we must assert $I(\lambda^2)p(\lambda^2)w(\lambda^2)$ is a real-valued function (by construction, assuming the weight function is strictly real) with $e^{2i\pi\alpha}$ approximately constant (random around a mean) over the passband; $F(\phi) * R(\phi)$ must be hermitian. This is necessary to restrict the integral to the domain $[0, \infty]$, since the contribution induced on the integral by $-iU\sin(-u\pi) = iU\sin(u\pi)$ is symmetric under this assumption.

Assuming $\Delta\lambda \ll \lambda$, the integral can be approximated by a discrete Fourier transform given by the matrix D:

$$(-0.5\phi_{\text{sup}}/\Delta\phi \leq x \leq 0.5\phi_{\text{sup}}/\Delta\phi)\ D := e^{-2i(\Delta\phi x \otimes \lambda^2)}$$

$$= \begin{bmatrix} e^{-2i\pi u_0\phi_0} & e^{-2i\pi u_1\phi_0} & \dots & e^{-2i\pi u_N\phi_0} \\ e^{-2i\pi u_0\phi_1} & e^{-2i\pi u_1\phi_1} & \dots & e^{-2i\pi u_N\phi_1} \\ \vdots & \vdots & \ddots & \vdots \\ e^{-2i\pi u_0\phi_M} & e^{-2i\pi u_1\phi_M} & \dots & e^{-2i\pi u_N\phi_M} \end{bmatrix}$$

To improve SNR, an average for Q and U is computed (assuming they have been corrected for leakage and parallactic angle rotation), then the average Faraday dispersion vector, of shape M, can be computed as

$$F(\phi) = DP_{\text{measured}}$$

Further, $\Delta\phi$ is given by Nyquist criterion:

$$\Delta\phi \leq \frac{1}{2\max(\Delta u)\pi N_{\text{chan}}}$$

The support in ϕ is (assuming F engine channelization response is a boxcar):

$$\phi_{\text{sup}} \approx \frac{\sqrt{3}}{\min(\Delta\lambda^2)}$$

Provided there is sufficient SNR on the source the angle can be recovered as:

$$\rho_{\text{intrinsic}} = \rho_{\text{apparent}}(\lambda^2) - 2\lambda^2 \text{argmax}(F(\phi))$$

5 Observation and calibration requirements

Our polarization analysis is performed using observations 1517882072 and 1517940096 taken February 6, 2018. Some of which had integration intervals of up to 8 seconds, making the observations unsuitable for widefield imaging due to time smearing. PKS 1934-638, 3C286, 3C138 and PKS 0407-65 were observed.

The calibration procedure involved solving for bandpass and gains using PKS 1934-638 and transferring those to all other calibrator fields. The [Reynolds, 1994] model is included in CASA and used to set the flux scale. We solved for differential phase gains for all fields, but crucially we did not adjust the amplitudes of any of these fields.

We used integrated spectra coefficients from [Perley and Butler, 2017] for 3C286 and 3C138, and used L-Band polarization characteristics from the NRAO polarization guide [1].

The crosshand delays were solved for using 3C286 and 3C138. The polarization angles were solved for using 3C286 alone and crosschecked in section 7.2. Importantly, note that antenna m059 was used as reference antenna throughout calibration. 3C286 thus serves as reference for absolute polarization angle. As for the crosshand delays, the only requirement imposed is to use a highly polarized source to solve for these delays at regular intervals due to SNR requirements on the crosshand visibilities. Leakages are calculated using the unpolarized PKS 1934-638.

We used the following heuristic to determine the necessary solution intervals needed to obtain desired SNR on solutions:

$$\Delta\tau = \frac{(\mathrm{SEFD} \times 10^{\mathrm{dB}_\sigma/10})^2}{2 \times S^2 \times \Delta\nu \times (N_{\mathrm{ant}} - 1)} / 60 \text{ [mins]}$$

Assuming worst case SEFD of 578 Jy, obtaining -30dB stability per 208kHz channel with 16 antennae can be achieved in 3.91 minutes. We normally assume intervals of 20+ minutes to account for RFI. We used gain solution intervals of 3 minutes for similar reasons, although the desired SNR can theoretically be achieved in under a second if half the band is averaged. We also perform a second round of RFI excision based on Stokes Q, U and V.

Since 3C286 is roughly 9.5% polarized, longer solution intervals are needed when computing crosshand phase solutions. We estimate that the differential changes in phase can be computed in under 2 seconds at the reference frequency, however channelization of 208kHz would require 42mins for solving for frequency-dependent solutions. Averaging to a resolution of 4 channels these solutions can be computed at intervals of 10.6 minutes.

The second half of the modelling process entails creating a model of the substructure of the field. To achieve this we relied on observations 1522062927 and 1522070487 taken 26 March 2018 (using the ROACH2 system). This time PKS 0407-65, PKS 1934-638 and 3C138 were observed. A drift in crosshand delays, lasting more than an hour was seen in the observation of 3C138. m041 had to be flagged due to large phase closure issues. Additionally m000 and m011 had low power for nearly 1 hour of the observation of PKS 1934-638. Preliminary indications are that a faulty switch could be at fault [2].

As with the first observation we used PKS 1934-638 to set the flux scale of the instrument. Since PKS 0407-65 and PKS 1934-638 has roughly the same declination (albeit separated by several hours in right-ascension we assume that flux biases due to sidelobe contribution are minimal. Leakages were again corrected using PKS 1934-638. These observations did not have the same quality in general as the observations taken in February and was not used in modeling the polarization of PKS 0407-65.

6 Integrated source spectrum

We used the Reynolds model [Reynolds, 1994] to set the flux scale of our bandpass calibrator PKS 1934-638, a Gigahertz-peaked source with turnover point near the centre of the MeerKAT passband. These solutions were used to bootstrap the fluxscale of PKS 0407-65. We then fitted a third-order log polynomial through the median of the visibilities after subtracting the substructure sources[3] listed in Appendix A. The central source dominates the visibilities and it is more accurate

[1] Located here: https://science.nrao.edu/facilities/vla/docs/manuals/obsguide/modes/pol
[2] Sharmila priv. communication
[3] Thanks to Tom Mauch for pointing out this error in an earlier draft of this report

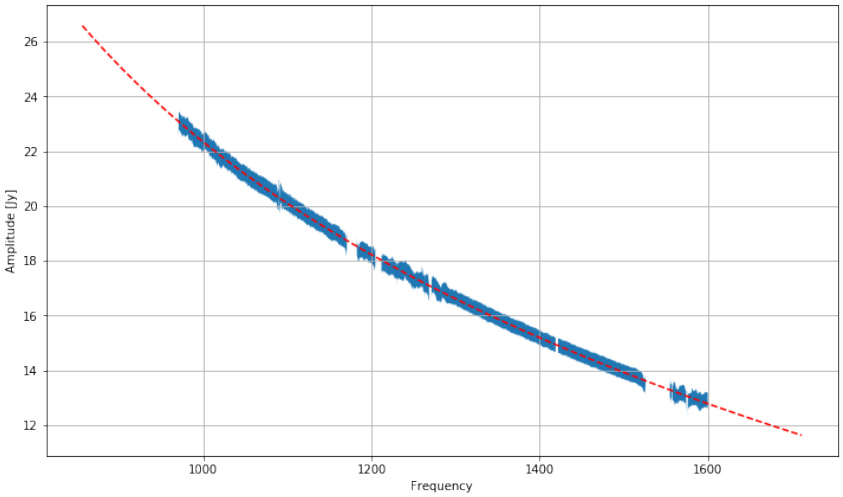

Figure 3: Fitted integrated source spectrum of PKS0407-65. The interquartile spread of the Stokes I component is shown in blue.

to fit in the visibilities rather compared to, say, 3-4 Multi-Frequency Synthesis image bands. The fit is plotted in Figure 3. We used the following convention in defining the log-polynomial:

$$
\begin{aligned}
I(\nu) &= I(\nu_0)\left(\frac{\nu}{\nu_0}\right)^{\alpha+\beta\ln\left(\frac{\nu}{\nu_0}\right)+\gamma\ln^2\left(\frac{\nu}{\nu_0}\right)} \\
\nu_0 &= 1.4 \text{ GHz} \\
I(\nu_0) &= 15.19200487458442 \pm 2.93336224e^{-6} \text{ Jy} \\
\alpha &= -1.2309337662992943 \pm 1.09001728e^{-6} \\
\beta &= -0.4014254868427545 \pm 1.05480069e^{-4} \\
\gamma &= -0.4272505074440009 \pm 6.61818440e^{-4}
\end{aligned}
$$

7 Polarization properties

7.1 Leakage correction using PKS 1934-638

Solving for leakage (**D**) terms is done using the Gigahertz-peaked source PKS 1934-638. We define total leakage as (on an unpolarized source):

$$D_{\text{tot}} := \frac{\sqrt{Q^2+U^2+V^2}}{I}$$

PKS 1934-638 is known to be unpolarized. After correcting for the bandpass and electronic gains (**BG**) the boresight leakages are at the ≈ -30dB (0.1%) level across most of the passband. The residual peaks, in particular the 1.15 to 1.3GHz region, is broadband RFI stemming from GPS and GLONAS satellite. After correction, leakages improve to the -36 to -39dB (0.025% to 0.013%) level (GSF: I don't think I understand the pre-/post-leakage correction. Are you solving for D with PKS 1934 and then applying that solution back to the same data? If so, then you are showing that there is a limit to the S/N at the -36 dB level. That is useful to show, but those values shouldn't be taken seriously as the true leakage limits). We estimate that the residual calibration error is well-within 0.5% of Stokes I, by assuming that Stokes V contains only noise and residual RFI. See Figure 4.

7.2 Crosschecking 3C286

Modelling 0407-65 entails establishing the intrinsic polarization angle of the source. In the first order polarization calibration approach we have followed here we have corrected delay and phase

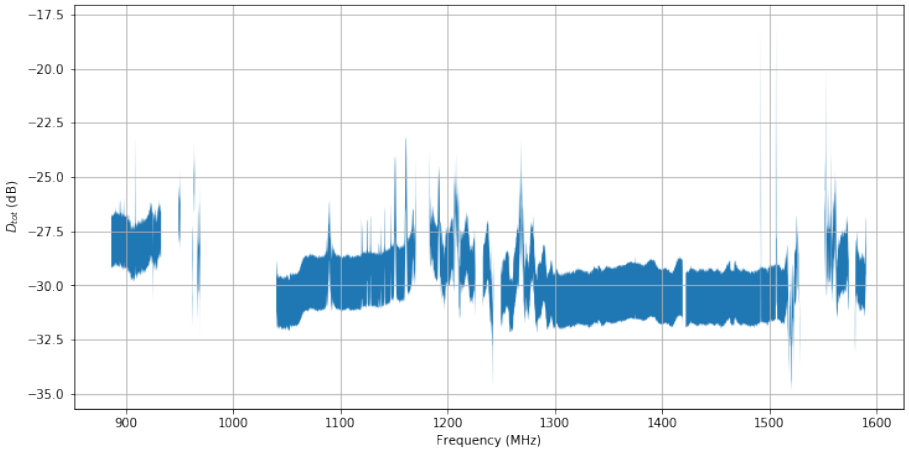

(a) Pre-leakage correction

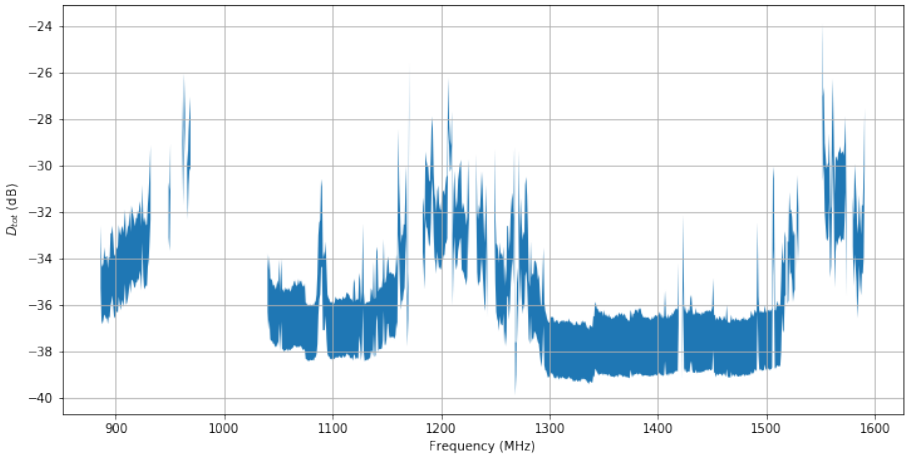

(b) Post-leakage correction

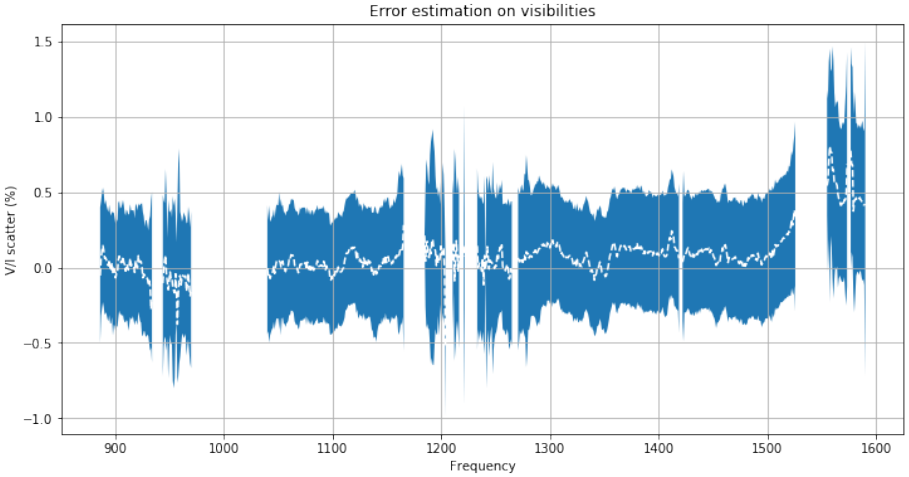

(c) Estimated error as a fraction of Stokes I

Figure 4: Leakage correction using unpolarized PKS 1934-638. Here we have averaged to 832kHz channelization. The mean + 1std deviation is plotted in the filled regions. Stokes V is used for estimating residual calibration error. Here the interquartile range is plotted as filled region and the median as white dashed line.

with respect to a reference antenna. The same reference antenna is used to calculate the absolute phase offset between the crosshand feeds with respect to a known polarized celestial source. A key assumption that is made is that the feeds of that antenna is nominally aligned. We therefore first have to establish that the corrected visibilities are correctly calibrated to account for parallactic angle and that the sign convention for Q and U can be tied to reference instruments such as the WSRT.

The sign convention for the HV feeds in MeerKAT are flipped, either by a bug in the correlator or in KATdal. It is necessary to rotate the converted X and Y feeds by $\pi/2$[4] and to flip the sign for Q. The resulting corrected data for 3C286 then corresponds to corrected data obtained with WSRT at 21CM in 72m configuration (archive project 11202121), as is shown in Figure 5. In calibrating the WSRT dataset we have used 3C48 as bandpass and leakage calibrator with fluxdensity and spectral model taken from [Perley and Butler, 2017]. 3C48 is unpolarized. The recovered polarization fraction is 9.641[5] at Faraday depth of 4.610 ($\pm$0.922) rad m^{-2}. The recovered intrinsic polarization angle lies between 0.25° and 1.75°.

After correcting for the HV-feed convention used in MeerKAT the correct signs for Q and U are recovered. The fractions also correspond with the fraction of polarization recovered in the WSRT observation. The larger spread in Q and U is not due to incorrect parallactic angle derotation. See Figure 6. The RM synthesis results are plotted in 7.

7.3 A slightly polarized PKS 0407-65

The results of our analysis of the polarization properties of PKS 0407-65 are summarized in Figure 8. A clean part of the band in the 1.3 to 1.5 GHz region was picked to ensure the RM synthesis is not biased by noise. We find that the source is 0.543% polarized (thus roughly 5x higher than uncorrected leakages) with an angle that varies between $-40°$ and $-20°$ at a Faraday depth of -2.045 ± 2.043 rad m^{-2}.

It is important to note that taking the polarization properties of PKS 0407-65 correctly into account during calibration of XX and YY during differential electronic gain and bandpass calibration, it is necessary to account for the effects of parallactic angle during the model prediction step. This can be achieved using Meqtrees [Noordam and Smirnov, 2010] or Montblanc [Perkins et al., 2015]. At the moment the SDP calibration pipeline does not correct for parallactic angle.

8 Field substructure

8.1 Modeling the field substructure

To create an apparent local sky model of the field surrounding PKS 0407-65 we used WSClean [Offringa et al., 2014] to create a 2°13′ widefield-wideband image with 5 MFS bands. Since the model is to be used only for calibrating MeerKAT it is not necessary to do beam corrections,. A beam-corrected intrinsic image can be created using DDFacet [Tasse et al., 2017] for comparison to intrinsic-scale catalogs and other instruments if needed in the future.

We fitted for source positions and shape (gaussians) using pyBDSF [Mohan and Rafferty, 2015]. The apparent spectra was fitted using the MFS model cube convolved with a 5 pixel circular gaussian to avoid biases introduced by the differences in scale of the CLEAN beam over the wide MeerKAT bandwidth.

A phase and amplitude direction-independent calibration was performed using the Meqtrees [Noordam and Smirnov, 2010] to predict and CASA [McMullin et al., 2007] to calibrate, using the full sky model at integration intervals of 13.312 MHz and 5 minutes. The resulting MFS image is shown in Figure 9. The sky model was refitted by repeating the process outlined above and is included as Appendix A.

8.2 Effects of not including substructure

In an earlier memo we have established that not including substructure in the model of PKS 1934-638 will induce ripples on the order of 3/1000 (-25dB) if short solution intervals of 64s intervals

[4] Nadeem Oozeer, private communication

[5] Although the fraction is provided in the model for 3C286 only the phase of the crosshands are calibrated. The fraction represented here is an independent measure of polarization power

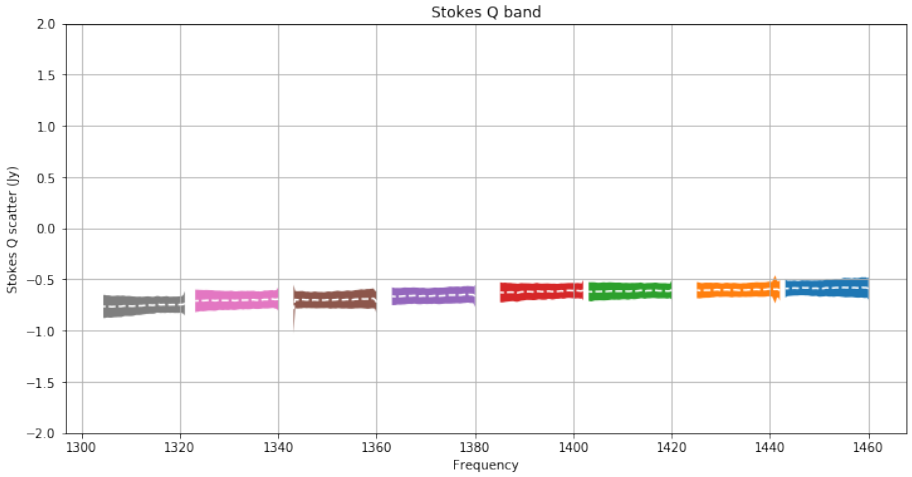

(a) Spread in Stokes Q. Colorized by spectral window.

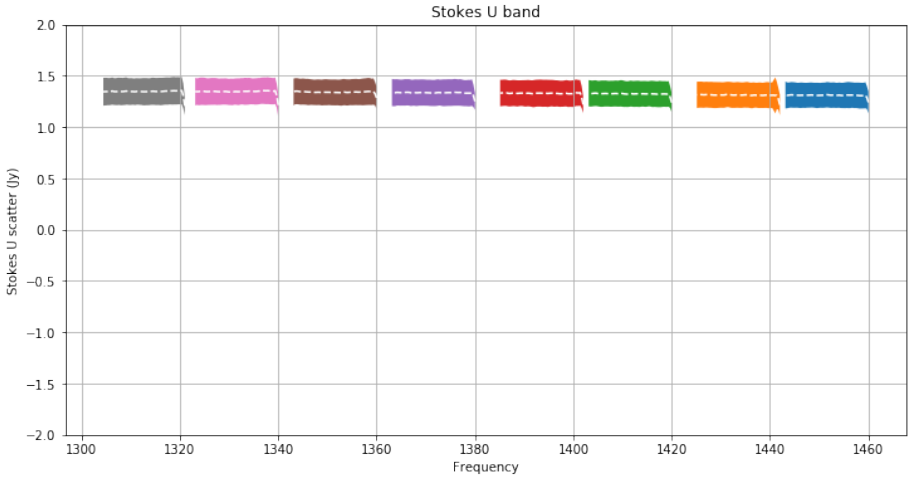

(b) Spread in Stokes U. Colorized by spectral window.

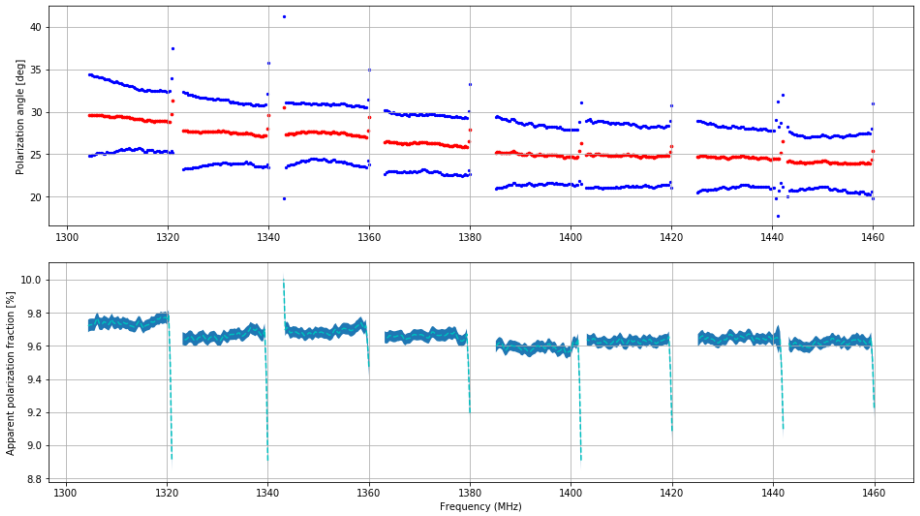

(c) Apparent polarization angle and fraction. Blue dots indicate 1 std deviation in Q/U fraction in in the case of polarization angle. Stokes V scatter is plotted around mean apparent polarization fraction.

Figure 5: Corrected data for 3C286 obtained with WSRT in 72cm configuration. The correct angle and fraction is recovered considering an apparent model with polarization angle of 33° is used and it is known that 3C286 is roughly 9.5% polarized.

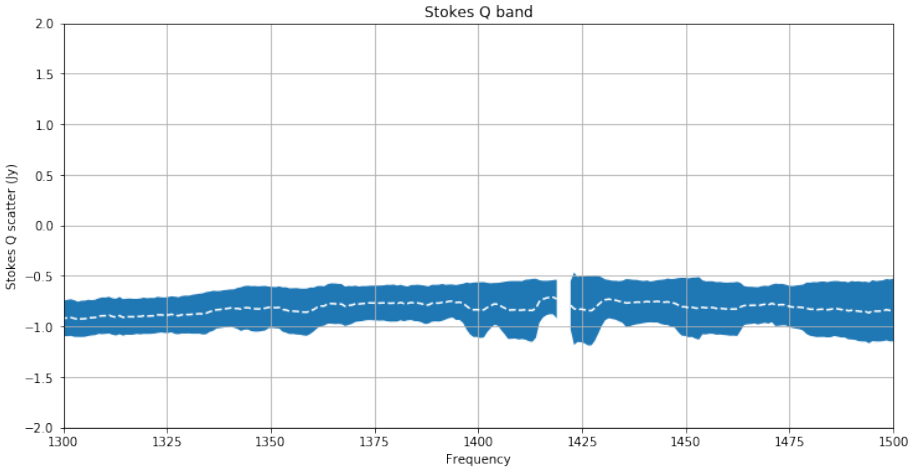

(a) Spread in Stokes Q. For comparison purposes the a subband of data is plotted.

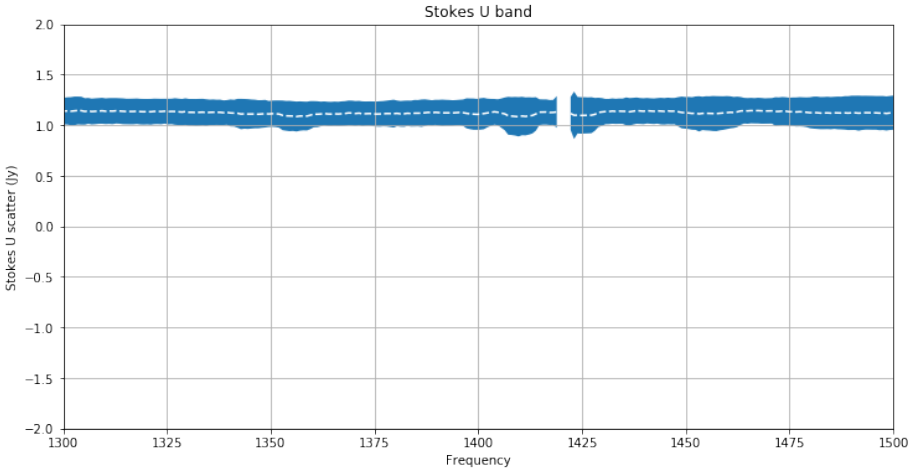

(b) Spread in Stokes U. For comparison purposes the a subband of data is plotted.

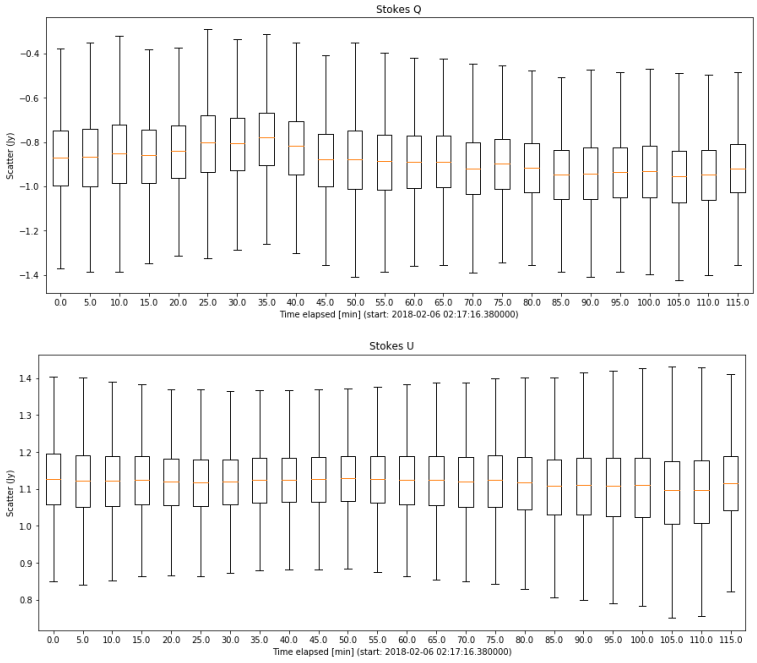

(c) Corrected Q and U after corrections for parallactic angle has been applied.

Figure 6: Corrected data for 3C286 obtained with MeerKAT. The signs and magnitudes of Q and U correspond to the apparent values obtained with WSRT.

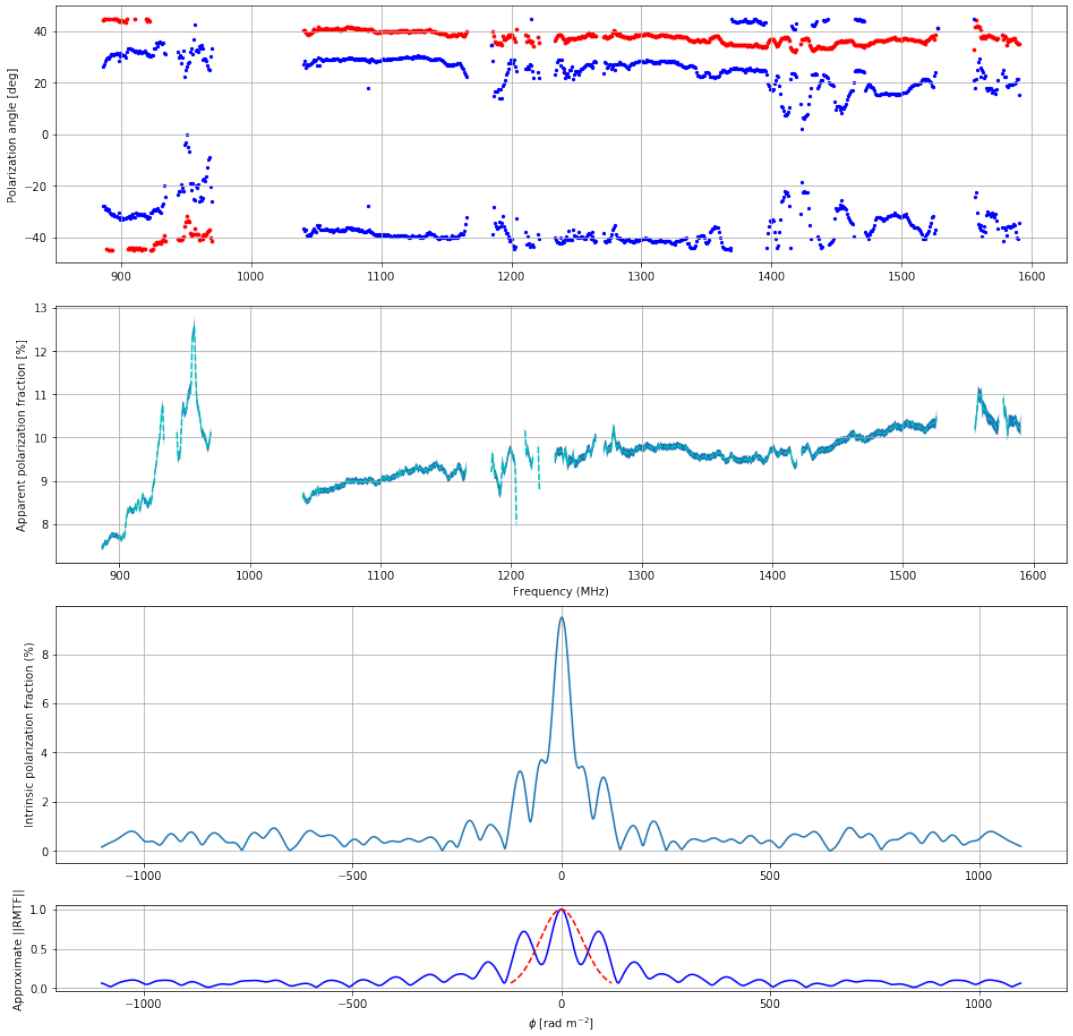

Figure 7: RM synthesis using channelization of 832kHz. The angle recovered is approximately correct consisidering the spread in the Q/U fraction. We have also plotted the Rotation Measure Transfer Function and FWHM in red dashed lines in the bottom plot if all channels were to be weighed equally. We weighed the channels by the number of flags during the course of the observation to compute a better estimation of the RMTF. RM synthesis recovers a polarization fraction of 9.499 % at a Faraday depth of 2.045 (+/- 2.043) rad m^{-2}

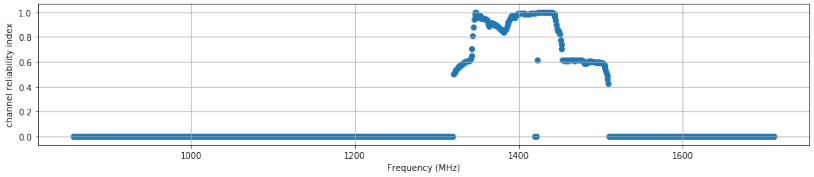

(a) Fraction of unflagged data points per channel

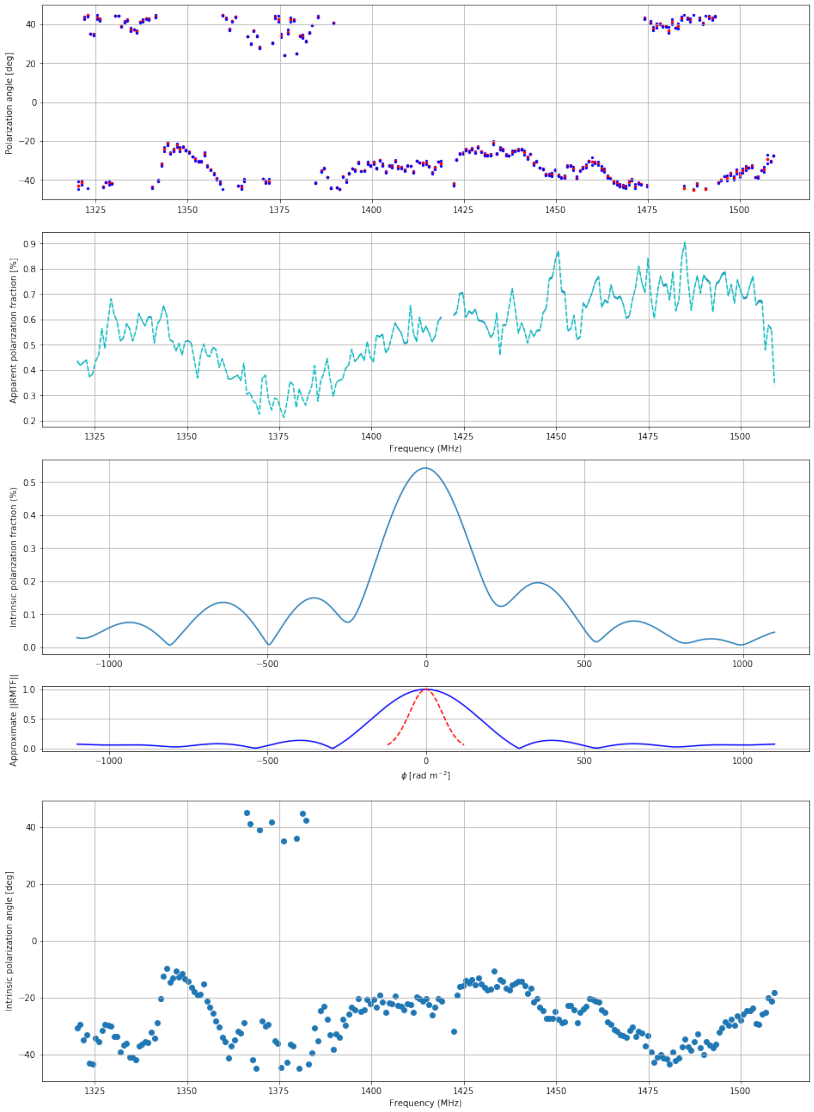

(b) Apparent polarization angle, fraction, recovered intrinsic polarization fraction and angles, and approximate RMTF are plotted for selected channel range. Scatter on apparent angle is plotted in blue.

Figure 8: RM synthesis for PKS0407-65

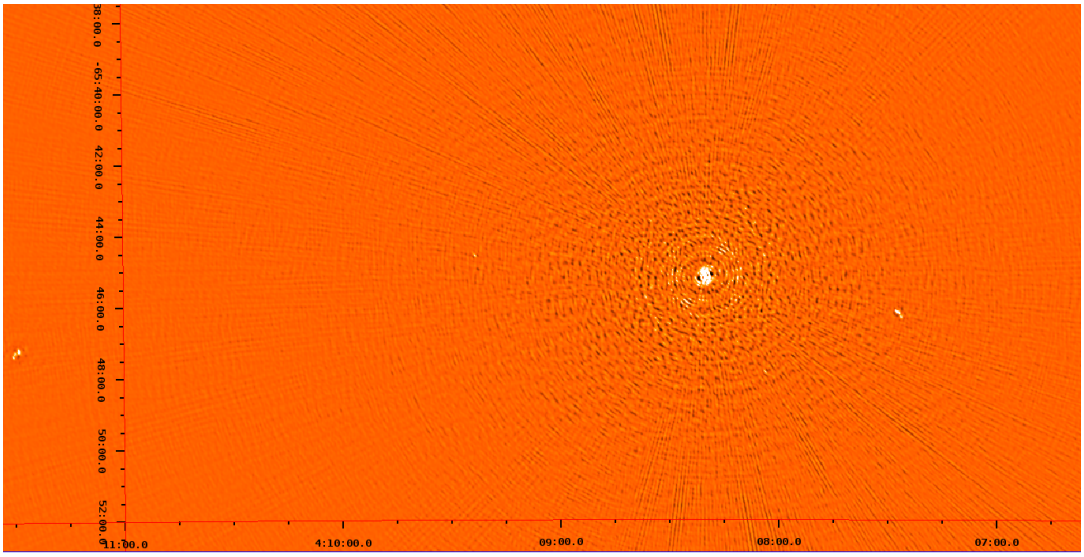

Figure 9: Close-up of substructure near PKS 0407-65. We estimate that the noise close to the source is roughly 2.3 mJy. Beyond the 5' distance the noise goes down to about 1 mJy. The image dynamic range is sufficient to capture sub-percent-level substructure.

are used. In that case there was a source of 27mJy (0.18%, apparent) 12' away from the central source. One of the criticisms noted was that one would expect this effect to diminish with longer solution intervals on the calibrator field due of bandwidth and time smearing.

In the case of PKS 0407-65 the situation is much worse. We have detected a bright double lobed source 1% (integrated flux) level 5'32" away of the central source. To see what effect the substructure has on computed bandpass solutions we ran several simulations using the Meqtrees [Noordam and Smirnov, 2010] framework and calibrating with CASA [McMullin et al., 2007]. We predicted a full sky model and then calibrated using only the central source in the calibration model at various solution intervals. The aim is to establish whether the substructure of sources this close to the central source would wash out. To isolate the effect of field substructure on the bandpass solutions these simulations excluded noise and the integrated spectra of the central and substructure sources. The results are plotted in Figure 10.

This indicates that even with very long intervals the errors induced on the bandpass solutions are above the 1% level. These errors are an order of magnitude above any errors induced by expected system leakages.

9 Conclusion

Our investigation of one of the primary MeerKAT calibrators, PKS 0708-65, reveiled that the source is polarized at the 0.5% level at low Faraday depth. The field also contains substructure at the 1% level to the primary calibrator source. We have shown that failure to take these properties of the calibrator field into account will introduce errors that are, respectively, 5 times and an order of magnitude higher than the leakage effects resulting from coupling between feeds. A new model is derived that should be included within the SDP calibration pipeline to ensure spectral line and, more importantly, pulsar timing observations are calibrated correctly.

References

[Brentjens and De Bruyn, 2005] Brentjens, M. A. and De Bruyn, A. (2005). Faraday rotation measure synthesis. *Astronomy & Astrophysics*, 441(3):1217–1228.

[Burn, 1966] Burn, B. (1966). On the depolarization of discrete radio sources by faraday dispersion. *Monthly Notices of the Royal Astronomical Society*, 133(1):67–83.

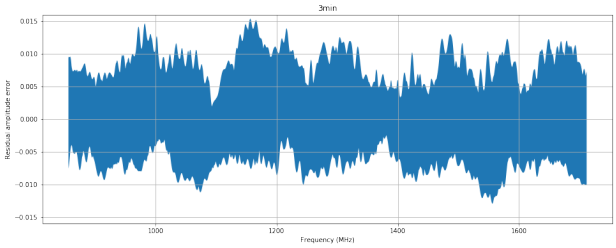

(a) 3 minute intervals

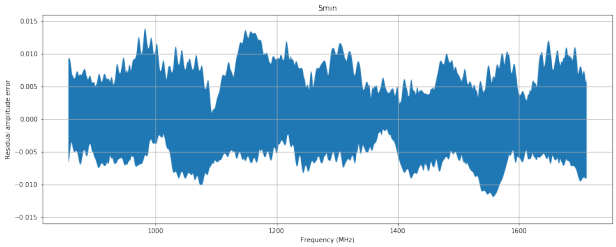

(b) 5 minute intervals

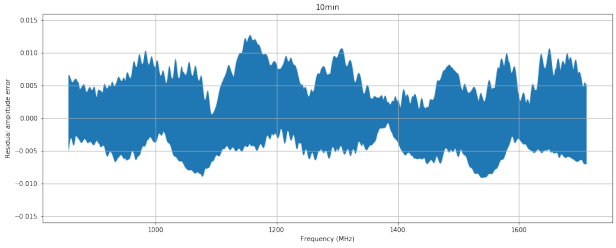

(c) 10 minute intervals

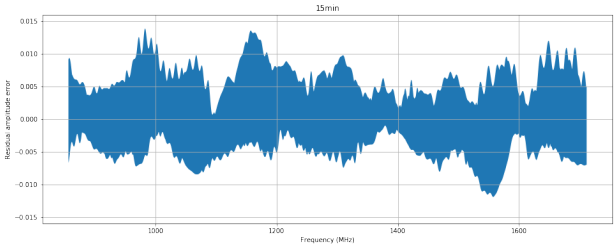

(d) 15 minute intervals

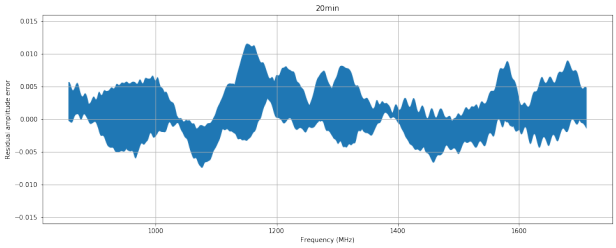

(e) 20 minute intervals

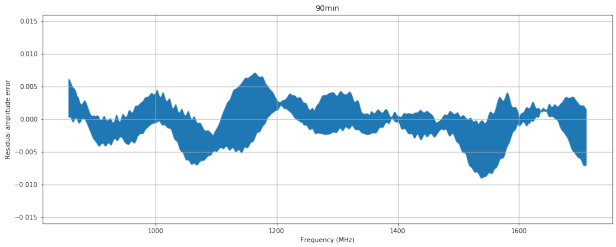

(f) 90 minute intervals

Figure 10: Simulation showing time variation in residual bandpass calibration errors, $1 - \mathbf{B}(\nu, \tau_{\text{centroid}})$, for a single antenna if substructure is ignored. The fine structure washes out over longer calibration intervals due to bandwidth and time smearing, but contribution from dominating nearby sources remain.

[Foster et al., 2015] Foster, G., Karastergiou, A., Paulin, R., Carozzi, T., Johnston, S., and van Straten, W. (2015). Intrinsic instrumental polarization and high-precision pulsar timing. *Monthly Notices of the Royal Astronomical Society*, 453(2):1489–1502.

[Hales, 2017] Hales, C. A. (2017). Calibration Errors in Interferometric Radio Polarimetry. *The Astronomical Journal*, 154:54.

[McMullin et al., 2007] McMullin, J., Waters, B., Schiebel, D., Young, W., and Golap, K. (2007). Casa architecture and applications. In *Astronomical data analysis software and systems XVI*, volume 376, page 127.

[Mohan and Rafferty, 2015] Mohan, N. and Rafferty, D. (2015). Pybdsf: Python blob detection and source finder. *Astrophysics Source Code Library*.

[Noordam and Smirnov, 2010] Noordam, J. E. and Smirnov, O. M. (2010). The meqtrees software system and its use for third-generation calibration of radio interferometers. *Astronomy & Astrophysics*, 524:A61.

[Offringa et al., 2014] Offringa, A., McKinley, B., Hurley-Walker, N., Briggs, F., Wayth, R., Kaplan, D., Bell, M., Feng, L., Neben, A., Hughes, J., et al. (2014). Wsclean: an implementation of a fast, generic wide-field imager for radio astronomy. *Monthly Notices of the Royal Astronomical Society*, 444(1):606–619.

[Perkins et al., 2015] Perkins, S., Marais, P., Zwart, J., Natarajan, I., Tasse, C., and Smirnov, O. (2015). Montblanc1: Gpu accelerated radio interferometer measurement equations in support of bayesian inference for radio observations. *Astronomy and Computing*, 12:73–85.

[Perley and Butler, 2017] Perley, R. A. and Butler, B. J. (2017). An accurate flux density scale from 50 mhz to 50 ghz. *The Astrophysical Journal Supplement Series*, 230(1):7.

[Reynolds, 1994] Reynolds, J. (1994). A revised flux scale for the at compact array. *ATNF Internal*.

[Smirnov, 2011] Smirnov, O. M. (2011). Revisiting the radio interferometer measurement equation-i. a full-sky jones formalism. *Astronomy & Astrophysics*, 527:A106.

[Tasse et al., 2017] Tasse, C., Hugo, B., Mirmont, M., Smirnov, O., Atemkeng, M., Bester, L., Bonnassieux, E., Hardcastle, M., Lakhoo, R., Girard, J., et al. (2017). Facetting for direction-dependent spectral deconvolution. *arXiv preprint arXiv:1712.02078*.

A Apparent model of PKS 0407-65

The following source catalog of PKS 0407-65 was created for the purposes of improving gain stability. Note that in this model both the brightness (Jy) and spectral slope and curvature is apparent and should only be used as a local sky model for calibrating MeerKAT:

name	RA_h	RA_m	RA_s	DEC_d	DEC_m	DEC_s	i	$emaj_s$	$emin_s$	pa_d	ν_0	α	β	γ
PKS0407-65	04	08	20.380	-65	45	09.08	15.19200487458442	0	0	0	1.4e9	-1.2309337662992943	-0.4014254868427545	-0.4272505074440009
B260	4	7	27.75	-65	46	8.73000000001	0.122542605147	0.0	0.0	0.0	1300000000.0	-0.963704594818	0.0	0.0
C101	4	11	28.73	-65	47	9.61000000002	0.128190166362	0.0	0.0	0.0	1300000000.0	-1.63033458075	0.0	0.0
D303	4	4	7.1	-65	29	27.7	0.0861983891848	0.0	0.0	0.0	1300000000.0	-2.10095563429	0.0	0.0
B260a	4	7	27.1	-65	46	10.35	0.105791687419	0.0	0.0	0.0	1300000000.0	-1.16306396402	0.0	0.0
C101a	4	11	28.86	-65	47	12.36	0.0706836472104	0.0	0.0	0.0	1300000000.0	-1.76848807102	0.0	0.0
C101b	4	11	30.26	-65	47	19.78	0.0374241037283	0.0	0.0	0.0	1300000000.0	-1.20344298815	0.0	0.0
B260b	4	7	26.53	-65	46	17.12	0.0302530220026	0.0	0.0	0.0	1300000000.0	-1.51131649711	0.0	0.0
E083	4	14	0.25	-65	37	30.35	0.0231058331639	0.0	0.0	0.0	1300000000.0	-1.64087549871	0.0	0.0
F080	4	9	23.46	-65	44	33.58	0.0224000447262	0.0	0.0	0.0	1300000000.0	-1.83976568001	0.0	0.0
C101c	4	11	29.77	-65	47	14.01	0.0431619047108	0.0	0.0	0.0	1300000000.0	-1.81678308534	0.0	0.0
H121	4	10	45.28	-65	54	19.72	0.0223934091758	0.0	0.0	0.0	1300000000.0	-1.43339035721	0.0	0.0
J294	4	1	59.58	-65	30	9.23000000001	0.0164218428383	0.0	0.0	0.0	1300000000.0	-2.55893081143	0.0	0.0
C101d	4	11	28.77	-65	47	6.91	0.0965801842051	0.0	0.0	0.0	1300000000.0	-1.47496269887	0.0	0.0
K153	4	11	11.11	-66	18	49.08	0.022044213962	0.0	0.0	0.0	1300000000.0	-2.59795371862	0.0	0.0
M171	4	8	47.28	-65	56	0.600000000006	0.0122532345948	0.0	0.0	0.0	1300000000.0	0.0693727497313	0.0	0.0
C101e	4	11	30.03	-65	47	16.3	0.042727651569	0.0	0.0	0.0	1300000000.0	-1.49545760179	0.0	0.0
N263	4	3	22.18	-65	52	56.45	0.0124031141893	0.0	0.0	0.0	1300000000.0	-2.20115077193	0.0	0.0
O012	4	9	6.15	-65	17	33.77	0.00870665698799	0.0	0.0	0.0	1300000000.0	-1.62655742374	0.0	0.0
P183	4	8	34.22	-66	21	40.19	0.00848219347426	0.0	0.0	0.0	1300000000.0	-2.2864486946	0.0	0.0
D303a	4	4	7.34	-65	29	29.22	0.0505750354093	0.0	0.0	0.0	1300000000.0	-2.14890817951	0.0	0.0
K153a	4	11	10.83	-66	18	50.18	0.0210588347674	0.0	0.0	0.0	1300000000.0	-2.62245396315	0.0	0.0
Q034	4	12	38.3	-65	5	32.0	0.00448427092077	0.0	0.0	0.0	1300000000.0	-3.5198146301	0.0	0.0
R324	4	4	22.64	-65	10	12.35	0.00471858050117	0.0	0.0	0.0	1300000000.0	-3.22015109964	0.0	0.0
S322	4	5	25.69	-65	23	29.94	0.00573539522462	0.0	0.0	0.0	1300000000.0	-1.3679697352	0.0	0.0
T333	4	5	8.06	-65	14	28.85	0.00411783206993	0.0	0.0	0.0	1300000000.0	-2.90483061823	0.0	0.0
U245	4	0	33.0	-66	8	35.97	0.00383307561615	0.0	0.0	0.0	1300000000.0	-2.96319185969	0.0	0.0
H121a	4	10	45.37	-65	54	24.35	0.00699479540349	0.0	0.0	0.0	1300000000.0	-1.32261983685	0.0	0.0
C101f	4	11	29.42	-65	47	12.68	0.0491991658085	0.0	0.0	0.0	1300000000.0	-1.95490479783	0.0	0.0
C101g	4	11	28.34	-65	47	13.71	0.0667151061842	0.0	0.0	0.0	1300000000.0	-1.65943838577	0.0	0.0
V311	4	6	41.51	-65	36	13.59	0.00199330090771	0.0	0.0	0.0	1300000000.0	1.64366684153	0.0	0.0
W057	4	16	28.33	-64	55	48.0	0.00101665525648	0.0	0.0	0.0	1300000000.0	-5.81657749521	0.0	0.0
X332	4	5	37.03	-65	20	37.75	0.00133615751619	0.0	0.0	0.0	1300000000.0	0.0478217695041	0.0	0.0
K153b	4	11	6.95	-66	18	40.63	0.000490610496382	0.0	0.0	0.0	1300000000.0	-3.32550113669	0.0	0.0
Q034a	4	12	41.58	-65	5	41.55	0.000455183992957	0.0	0.0	0.0	1300000000.0	-3.35726605227	0.0	0.0
Y162	4	9	55.94	-66	10	34.7	0.00041910900189	0.0	0.0	0.0	1300000000.0	-4.05105518226	0.0	0.0
Y162a	4	9	55.86	-66	10	38.87	0.000180962334881	0.0	0.0	0.0	1300000000.0	-4.05105522388	0.0	0.0
D303b	4	4	6.63	-65	29	27.91	0.0658123178367	0.0	0.0	0.0	1300000000.0	-2.03520748724	0.0	0.0
N263a	4	3	22.08	-65	52	54.98	0.0132766078723	0.0	0.0	0.0	1300000000.0	-2.2130722273	0.0	0.0
ab203	4	6	18.63	-66	16	17.69	0.000632239452163	0.0	0.0	0.0	1300000000.0	-3.20290213863	0.0	0.0
C101h	4	11	28.27	-65	47	9.20999999999	0.0846346400126	0.0	0.0	0.0	1300000000.0	-1.62203627748	0.0	0.0
D303c	4	4	7.59	-65	29	25.24	0.0276248917377	0.0	0.0	0.0	1300000000.0	-2.12756125066	0.0	0.0
ab203a	4	6	18.47	-66	16	15.96	0.000948311975283	0.0	0.0	0.0	1300000000.0	-3.18747850839	0.0	0.0
ah347	4	3	51.72	-64	40	24.65	0.00134563714323	0.0	0.0	0.0	1300000000.0	-6.93037934426	0.0	0.0
ab203b	4	6	18.13	-66	16	18.94	0.000568377552778	0.0	0.0	0.0	1300000000.0	-3.21739881153	0.0	0.0
ah347b	4	3	52.03	-64	40	22.62	0.00109791097867	0.0	0.0	0.0	1300000000.0	-6.92756384239	0.0	0.0
ah347c	4	3	51.89	-64	40	26.08	0.000955958686282	0.0	0.0	0.0	1300000000.0	-6.93281990622	0.0	0.0
ah347d	4	3	51.83	-64	40	21.39	0.00120487688518	0.0	0.0	0.0	1300000000.0	-6.92441439675	0.0	0.0
C101i	4	11	30.32	-65	47	17.21	0.0392790226372	0.0	0.0	0.0	1300000000.0	-1.28100196121	0.0	0.0
ah347f	4	3	51.66	-64	40	29.4	0.000215796203655	0.0	0.0	0.0	1300000000.0	-6.93657978342	0.0	0.0
ah347g	4	3	52.24	-64	40	19.55	0.000332105505587	0.0	0.0	0.0	1300000000.0	-6.92101148713	0.0	0.0
ah347h	4	3	51.47	-64	40	27.99	0.000519725757012	0.0	0.0	0.0	1300000000.0	-6.93488031107	0.0	0.0
ah347j	4	3	52.06	-64	40	18.14	0.000285921708346	0.0	0.0	0.0	1300000000.0	-6.91746789648	0.0	0.0